

International Journal of Modern Physics D
© World Scientific Publishing Company

IMPACT OF HYPERMAGNETIC FIELDS ON RELIC GRAVITATIONAL WAVES, NEUTRINO OSCILLATIONS AND BARYON ASYMMETRY

MAXIM DVORNIKOV

*Pushkov Institute of Terrestrial Magnetism, Ionosphere
and Radiowave Propagation (IZMIRAN),
108840 Moscow, Troitsk, Russia
mazdvo@izmiran.ru*

We study the evolution of random hypermagnetic fields (HMFs) in the symmetric phase of the early universe before the electroweak phase transition. The behavior of HMFs is driven by the analog of the chiral magnetic effect accounting for the asymmetries of leptons and Higgs bosons. These asymmetries are also dynamical variables of the model and evolve together with HMFs. Moreover, we account for the contribution of the hyper-MHD turbulence in the effective diffusion coefficient and the α -dynamo parameter. The realistic spectrum of seed HMFs consists of two branches: Batchelor and Kolmogorov ones. The impact of HMFs on the production of relic gravitational waves (GWs) and the baryon asymmetry of the universe (BAU), as well as flavor oscillations of supernova neutrinos in the stochastic GWs generated, are considered. We establish the constraint on the strength of the seed HMF comparing the spectral density of produced GWs with the observations of the LIGO-Virgo-KAGRA collaborations. The stronger upper bound on the seed HMF is obtained from the condition of not exceeding the observed value of BAU.

1. Introduction

The origin of cosmic magnetic fields is a puzzle for the modern astrophysics, cosmology, and particle physics. If one believes in the existence of nonzero magnetic fields in intergalactic voids, as suggested in Ref. 1, it is difficult to explain the production of such fields by astrophysical means. Thus large scale cosmic magnetic fields are likely to be of cosmological origin.² Cosmological magnetic fields with proper characteristics can be generated, e.g., during inflation, in the QCD and electroweak phase transitions (EWPT) and due to the Higgs field gradient. Some of the mechanisms for the production of such magnetic fields are reviewed in Ref. 3.

Maxwell cosmological magnetic fields can stem from hypermagnetic fields (HMFs) which exist before EWPT. These HMFs result from the massless hypercharge field Y^μ which is present in the symmetric phase of the universe evolution. A hypercharge field is a linear combination of electromagnetic and Z -boson fields. The connection between the production of HMFs and the leptogenesis, as well as the baryogenesis was suggested in Ref. 4. It is possible owing to the abelian anomaly for the hypercharge field. Thus, a configuration of HMFs decays and creates leptons

which are massless particles before EWPT. This scenario was further developed in Refs. 5, 6.

On the other hand, there is a backreaction from the lepton asymmetries to the evolution of (hyper)-magnetic fields. It is based on the chiral magnetic effect (the CME),⁷ which consists in the modification of the induction equation in the presence of a chiral imbalance, or an asymmetry, of ultrarelativistic fermions. A magnetic field becomes unstable in this case. The application of the CME is justified in the symmetric phase. However, one can use it in the broken phase as well⁸ by accounting for the appropriate spin flip rate.⁹

Besides the production of the baryon asymmetry of the universe (BAU), cosmological magnetic fields, which have a random structure, can result in the generation of relic gravitational waves (GWs). This problem was studied, e.g., in Ref. 10. The production of GWs in the primordial chiral plasma accounting for the CME was analyzed in Ref. 11. The recent interest to the studies of GW backgrounds of the cosmological origin¹² is inspired by the direct detection of GWs,¹³ as well as the claims (see, e.g., Ref. 14) that stochastic GWs can be achievable with modern GW detection techniques.

HMFs can indirectly influence neutrino oscillations. We found in Refs. 15, 16, 17 that neutrino flavor oscillations can be affected by stochastic GWs. Suppose that relic GWs are produced by HMFs, as described above. Then, these GWs interact with astrophysical neutrinos modifying the oscillations picture and changing their fluxes. Thus, we can say that the fluxes of astrophysical neutrinos are influenced by HMFs. Neutrino flavor oscillations in GWs were also considered in Ref. 18. The research on the interaction between neutrinos and GWs is inspired by various multimessenger studies,^{19,20} where both neutrinos and GWs are explored. Of course, existing neutrino telescopes are always waiting for a nearby supernova (SN),²¹ as well as trying to detect a SN neutrino background. It allows one to study the interaction between neutrinos and GWs.

This work is organized in the following way. We start in Sec. 2 with the formulation of the basic equations for the evolution of random HMFs. In Sec. 2.1, we set up the initial condition. We present the numerical solution of the evolution equations for the spectra and the asymmetries in Sec. 2.2. We study the generation of primordial GWs by HMFs in Sec. 3. The results of the GWs production are represented in Sec. 3.1. We also consider the possibility to observe the predicted GW background in Sec. 3.1. Neutrino flavor oscillations under the influence of relic GWs, generated in frames of our model, are discussed in Sec. 4. Finally, we study the production of BAU by the evolving asymmetries of particles in Sec. 5. In Sec. 6 we conclude. In Appendix A, we rederive the contribution of the (H)MHD turbulence to the effective diffusion coefficient and the α -dynamo parameter. We introduce the new variables for numerical simulations of the HMFs evolution in Appendix B. The expression for the function characterizing the energy spectrum of stochastic GWs is derived in Appendix C. In Appendix D, we clarify some of the issues in the derivation of the density matrix equation for flavor neutrinos interacting with stochastic

GWs.

2. Evolution of HMFs

The key issue in our study is the evolution of HMFs, as well as the lepton and Higgs boson asymmetries. This problem was considered in details in Refs. 22, 23.

We study the situation when HMFs evolve before EWPT. The behavior of HMFs accounts for the instability in the presence of nonzero particle asymmetries. The full set of the kinetic equations has the form,^{22,23}

$$\begin{aligned}
 \frac{\partial \tilde{\mathcal{E}}_{\text{BY}}}{\partial \tilde{\eta}} &= -2\tilde{k}^2 \eta_{\text{eff}} \tilde{\mathcal{E}}_{\text{BY}} + \alpha_{\text{eff}} \tilde{k}^2 \tilde{\mathcal{H}}_{\text{BY}}, \\
 \frac{\partial \tilde{\mathcal{H}}_{\text{BY}}}{\partial \tilde{\eta}} &= -2\tilde{k}^2 \eta_{\text{eff}} \tilde{\mathcal{H}}_{\text{BY}} + 4\alpha_{\text{eff}} \tilde{\mathcal{E}}_{\text{BY}}, \\
 \frac{d\xi_{eR}}{d\tilde{\eta}} &= -\frac{3\alpha'}{\pi} \int d\tilde{k} \frac{\partial \tilde{\mathcal{H}}_{\text{BY}}}{\partial \tilde{\eta}} - \Gamma(\xi_{eR} - \xi_{eL} + \xi_0), \\
 \frac{d\xi_{eL}}{d\tilde{\eta}} &= \frac{3\alpha'}{4\pi} \int d\tilde{k} \frac{\partial \tilde{\mathcal{H}}_{\text{BY}}}{\partial \tilde{\eta}} - \frac{\Gamma}{2}(\xi_{eL} - \xi_{eR} - \xi_0) - \frac{\Gamma_{\text{sph}}}{2} \xi_{eL}, \\
 \frac{d\xi_0}{d\tilde{\eta}} &= -\frac{\Gamma}{2}(\xi_{eR} + \xi_0 - \xi_{eL}),
 \end{aligned} \tag{2.1}$$

where $\tilde{\mathcal{E}}_{\text{BY}}(\tilde{k}, \tilde{\eta})$ and $\tilde{\mathcal{H}}_{\text{BY}}(\tilde{k}, \tilde{\eta})$ are the dimensionless spectral densities of the HMF energy and the helicity. The total densities of the energy and the helicity can be computed as $\tilde{B}_Y^2/2 = \int d\tilde{k} \tilde{\mathcal{E}}_{\text{BY}}(\tilde{k}, \tilde{\eta})$ and $\tilde{h} \equiv \int d^3x (\tilde{\mathbf{Y}} \tilde{\mathbf{B}}_Y)/V = \int d\tilde{k} \tilde{\mathcal{H}}_{\text{BY}}(\tilde{k}, \tilde{\eta})$, where $\tilde{\mathbf{Y}}$ is the hypercharge field in conformal variables and $\tilde{\mathbf{B}}_Y = (\nabla \times \tilde{\mathbf{Y}})$ is HMF. The dimensionless conformal time is $\tilde{\eta} = \tilde{M}_{\text{Pl}}(T^{-1} - T_{\text{RL}}^{-1})$ and the conformal momentum is $\tilde{k} = k_{\text{phys}}/T$, where $\tilde{M}_{\text{Pl}} = M_{\text{Pl}}/1.66\sqrt{g_*}$, T is the primeval plasma temperature, $T_{\text{RL}} = 10 \text{ TeV}$ is the temperature corresponding to the start of the evolution (see below), $M_{\text{Pl}} = 1.2 \times 10^{19} \text{ GeV}$ is the Planck mass, $g_* = 106.75$ is the number of the relativistic degrees of freedom before EWPT, and k_{phys} is the physical momentum.

Along with HMFs in Eq. (2.1), we account for the evolution of the asymmetries of right and left fermions $\xi_{eR,L} = 6(n_{eR,L} - n_{\bar{e}R,L})/T^3$, as well as that of Higgs bosons $\xi_0 = 3(n_{\varphi_0} - n_{\bar{\varphi}_0})/T^3$, where $n_{(e,\bar{e})(R,L)}$ are the number densities of right electrons, left fermions, their antiparticles, and $n_{\varphi_0, \bar{\varphi}_0}$ are the number densities of Higgs bosons and antibosons. As shown in Ref. 26, only the lightest lepton generation should be taken into account since other leptons are out of equilibrium sooner because their Yukawa coupling constants are greater. We demonstrated in Ref. 5 that left fermions are to be taken into account to transform Eq. (2.1) to the closed form.

Following Ref. 24, in Eq. (2.1), we assume that the global equilibrium in plasma before EWPT is characterized by five chemical potentials: μ_Y for the conserved hypercharge, μ_{eR} for right electrons, and three chemical potentials corresponding to three generations in the standard model. In Eq. (2.1), additionally we account for two chemical potentials of left leptons and Higgs boson to make our analysis

4 *Maxim Dvornikov*

self-consistent since we take into account the sphaleron processes. Our approach is different from that used in Ref. 6 where the evolution of all quarks asymmetries in the presence of HMFs was explicitly accounted for. In Refs. 22, 25, the evolution of HMFs and the BAU generation were studied on the basis of the approach proposed in Ref. 24.

In Eq. (2.1), the rate Γ is caused by the interaction of fermions with Higgs bosons. It was obtained in Ref. 26,

$$\Gamma(\tilde{\eta}) = \frac{242}{\tilde{\eta}_{\text{EW}}} \left[1 - \frac{\tilde{\eta}^2}{\tilde{\eta}_{\text{EW}}^2} \right], \quad \tilde{\eta}_{\text{EW}} = \frac{\tilde{M}_{\text{P1}}}{T_{\text{EW}}} = 7 \times 10^{15}, \quad (2.2)$$

where $T_{\text{EW}} = 10^2 \text{ GeV}$ is the temperature of EWPT. The dimensionless transitions rate due to the sphaleron processes can be taken as²⁷ $\Gamma_{\text{sph}} = 8 \times 10^{-7}$.

We suppose that the HMFs evolution starts at $T_{\text{RL}} = 10 \text{ TeV}$. This choice is justified by the fact that Higgs bosons decays become faster than the universe expansion below this temperature. Thus, the production of left fermions begins at $T < T_{\text{RL}}$. The maximal wave vector \tilde{k}_{max} , which is in the integration limits in Eq. (2.1), is related to the minimal length scale. It is the free parameter in our model. The strongest constraint on \tilde{k}_{max} results from the fact that the minimal scale should be greater than the Debye length to guarantee the plasma electroneutrality. In various parts of our work, we shall vary \tilde{k}_{max} in a quite broad range: $10^{-10} < \tilde{k}_{\text{max}} < 10^{-2}$. In this situation, the minimal length scale of HMFs is still greater than the conformal Debye length $\tilde{r}_{\text{D}} = 10$.

The effective magnetic diffusion coefficient η_{eff} and the effective α -dynamo parameter α_{eff} account for the analogs of both the CME and the (H)MHD turbulence for HMFs. They are²⁸ (see also Appendix A),

$$\begin{aligned} \eta_{\text{eff}} &= \sigma_c^{-1} + \frac{4(\alpha')^{-2}}{3} \frac{1}{\tilde{\rho} + \tilde{p}} \int d\tilde{k} \tilde{\mathcal{E}}_{\text{BY}}, \quad \alpha' = \frac{g'^2}{4\pi}, \\ \alpha_{\text{eff}} &= \alpha_{\text{Y}}(\tilde{\eta}) + \frac{2(\alpha')^{-2}}{3} \frac{1}{\tilde{\rho} + \tilde{p}} \int d\tilde{k} \tilde{k}^2 \tilde{\mathcal{H}}_{\text{BY}}, \end{aligned} \quad (2.3)$$

where $\sigma_c \approx 10^2$ is the conformal conductivity of a relativistic plasma, $\tilde{\rho}$ and \tilde{p} are the plasma density and the pressure expressed in conformal variables, $g' = e/\cos\theta_{\text{W}}$ is the hypercharge, and θ_{W} is the Weinberg angle. We choose $p = \rho/3$ for the ultrarelativistic plasma. The value of α' is $\alpha' = 9.5 \times 10^{-3}$.²²

Note that the form of α_{eff} in Eq. (2.3) is different from that in Refs. 22, 23, 29. To resolve the contradiction between the results of Ref. 28 and Ref. 29 we rederive the contribution of turbulent (H)MFs to the kinetic Eq. (2.1) in Appendix A; cf. Eq. (A.10). We confirm the validity of α_{eff} in Ref. 28. However, as mentioned in Refs. 22, 23 the evolution of HMFs does not depend significantly on the turbulent contribution to α_{eff} . Nevertheless, we use the correct α -dynamo parameter here.

The analog of the CME for HMFs is accounted for in α_{eff} in Eq. (2.3). We found in Ref. 5 that its contribution to the α -dynamo parameter depends on the

asymmetries of right and left leptons,

$$\alpha_Y(\tilde{\eta}) = \frac{\alpha'}{\pi\sigma_c} \left[\xi_{eR}(\tilde{\eta}) - \frac{\xi_{eL}(\tilde{\eta})}{2} \right]. \quad (2.4)$$

We use the correct sign in the left asymmetry term in Eq. (2.4). The most general expression for the α -dynamo parameter in Eq. (2.4) was found in Ref. 6 to contain the quarks contribution, $\sim \alpha' \times \text{BAU}/\pi\sigma_c$, in the right hand side, where the expression for BAU is given in Eq. (5.1) below. In our analysis, we neglect this term since it is smaller compared to the contribution of left and right electrons.

2.1. Seed spectrum of HMFs and initial asymmetries

The numerical analysis of Eq. (2.1) requires the initial condition for HMFs. In Refs. 22, 23, we took the Kolmogorov seed spectrum at T_{RL} . Thus, we had to impose the minimal momentum \tilde{k}_{min} to avoid the singularity of the Kolmogorov spectrum at $\tilde{k} = 0$. The value of \tilde{k}_{min} , which is associated to the maximal length scale, was taken to be the reciprocal horizon size at T_{RL} : $\tilde{k}_{\text{min}} \sim T_{\text{RL}}/\tilde{M}_{\text{Pl}} \approx 10^{-14}$.

However, as mentioned in Ref. 30, the spectrum of HMFs can be vanishing at distances greater than the horizon size. It leads to the composite seed spectrum,

$$\tilde{\mathcal{E}}_{\text{BY}}^{(0)}(\tilde{k}) \sim \begin{cases} \tilde{k}^{n_B}, & 0 < \tilde{k} < \tilde{k}_*, \\ \tilde{k}^{n_K}, & \tilde{k}_* < \tilde{k} < \tilde{k}_{\text{max}}, \end{cases} \quad (2.5)$$

i.e. $\tilde{\mathcal{E}}_{\text{BY}}^{(0)}(\tilde{k})$ is of the Batchelor type with $n_B = 4$ at small momenta, and $\tilde{\mathcal{E}}_{\text{BY}}^{(0)}(\tilde{k})$ is of the Kolmogorov type with $n_K = -5/3$ at great momenta. The border momentum \tilde{k}_* was found in Ref. 30 to be related to the reciprocal horizon size defined above: $\tilde{k}_* = T_{\text{RL}}/\gamma_*\tilde{M}_{\text{Pl}}$. We shall vary the parameter γ_* in the range $10^{-2} < \gamma_* < 10^{-3}$. The seed spectrum of the magnetic helicity can be taken in the form, $\tilde{\mathcal{H}}_{\text{BY}}^{(0)}(\tilde{k}) = 2q\tilde{\mathcal{E}}_{\text{BY}}^{(0)}(\tilde{k})/\tilde{k}$, where $0 \leq q \leq 1$ is the phenomenological parameter fixing the helicity of a seed HMF.

The normalization constant in the seed spectrum can be found using Eq. (2.5) and the new variables in Eq. (B.1),

$$\frac{\tilde{B}_0^2}{2} = \int_0^{\tilde{k}_{\text{max}}} \tilde{\mathcal{E}}_{\text{BY}}^{(0)}(\tilde{k}) d\tilde{k} = \frac{\pi^2 \tilde{k}_{\text{max}}^2}{6\alpha'^2} \left[C_B \int_0^{\kappa_*} \kappa^{n_B} d\kappa + C_K \int_{\kappa_*}^1 \kappa^{n_K} d\kappa \right], \quad (2.6)$$

where \tilde{B}_0 is the conformal seed HMF. Moreover, we request that the seed spectrum is continuous, i.e. $C_B \kappa_*^{n_B} = C_K \kappa_*^{n_K}$. These conditions define constants $C_{B,K}$. Finally, we get that the seed spectrum in the new variables in Eq. (B.1) reads

$$R_0(\kappa) = \frac{3\alpha'^2 \tilde{B}_0^2 (1 + n_K)}{\pi^2 \tilde{k}_{\text{max}}^2} \left(\frac{n_K - n_B}{1 + n_B} + \frac{1}{\kappa_*^{1+n_K}} \right)^{-1} \times \begin{cases} \frac{\kappa^{n_B}}{\kappa_*^{1+n_B}}, & 0 < \kappa < \kappa_*, \\ \frac{\kappa^{n_K}}{\kappa_*^{1+n_K}}, & \kappa_* < \kappa < 1, \end{cases} \quad (2.7)$$

where $\kappa_* = \tilde{k}_*/\tilde{k}_{\text{max}}$. Obviously that $0 < \kappa_* < 1$. The new helicity spectrum corresponding to Eq. (B.1) is $H_0(\kappa) = qR_0(\kappa)/\kappa$.

Besides the seed spectra, we should set the initial asymmetries in Eq. (2.1). We take that $\xi_{eL} = \xi_0 = 0$ and $\xi_{eR} = 10^{-10}$. It means that, if we study the BAU production in the system (see Sec. 5 below), the main contribution to BAU stems from the right electrons component. Analogous initial asymmetries were considered in Refs. 22, 23.

2.2. Numerical simulations of the HMF behavior

In this section, we present the numerical solution of Eq. (2.1) with the initial condition formulated in Sec. 2.1. For this purpose, we rewrite the system in the form in Eq. (B.2). We take that seed HMFs are maximally helical, i.e. $q = 1$. Indeed, we have shown in Refs. 22, 23 that the behavior of HMFs only slightly depends on q .

We demonstrate in Fig. 1 the spectra of the energy density $R \propto \tilde{\mathcal{E}}_{B_Y}$ and of the helicity density $H \propto \tilde{\mathcal{H}}_{B_Y}$ versus κ for different parameters of the system. We show both the seed spectra and the spectra at EWPT in Fig. 1. In particular, we fix γ_* and \tilde{k}_{\max} , and change $\tilde{B}_Y^{(0)}$ in Figs. 1(a) and 1(b); fix $\tilde{B}_Y^{(0)}$ and \tilde{k}_{\max} , and change γ_* in Figs. 1(c) and 1(d); and, finally, fix $\tilde{B}_Y^{(0)}$ and γ_* , and change \tilde{k}_{\max} in Figs. 1(e) and 1(f). Irregular parts of lines at the very great momenta $\kappa \lesssim 1$ are because of the inexactitude of numerical simulations.

We can see in Fig. 1 that the small momenta tails of the spectra are unchanged and coincide with the seed Batchelor spectra, which are also shown Fig. 1 by dashed lines. The Kolmogorov parts of the spectra, corresponding to great momenta, are mainly affected in the evolution. This behavior of the spectra qualitatively resembles that found in Ref. 23. It results from the fact that the major contribution to the evolution of HMFs is from the diffusion terms, $\propto -\kappa^2 R$ and $\propto -\kappa^2 H$, in the right hand side of Eq. B.2. The dynamo amplification of HMFs is not effective in the present system.

We show the evolution of the HMFs strength \tilde{B}_Y in Figs. 2(a), 2(c), and 2(e); as well as $\alpha_Y \propto \xi_{eR} - \xi_{eL}/2$ in Figs. 2(b), 2(d), and 2(f). The values of the parameters of the system in Fig. 2 are the same as in the corresponding panels in Fig. 1. Qualitatively, the evolution of \tilde{B}_Y and the asymmetries is similar to that described in Refs. 22, 23.

In particular, we can see in Figs. 2(a), 2(c), and 2(e) that the HMF strength becomes smaller in the cooling universe. It confirms our claim above that the dynamo amplification is not effective in this system. The α -dynamo parameter Figs. 2(b), 2(d), and 2(f) has a sharp peak at $T \lesssim T_{RL}$. This peak appears mainly owing to ξ_{eR} . It results from the term $\propto I_H$ in the right hand side of the equation for M_R in Eq. (B.2).

3. Production of primordial GWs

In this section, we study the generation of relic GWs by HMFs in the universe cooling down to EWPT. The main formalism for this problem was developed in Ref. 23. Here, we just remind the main steps of that study.

Impact of hypermagnetic fields on gravitational waves, neutrinos and baryon asymmetry 7

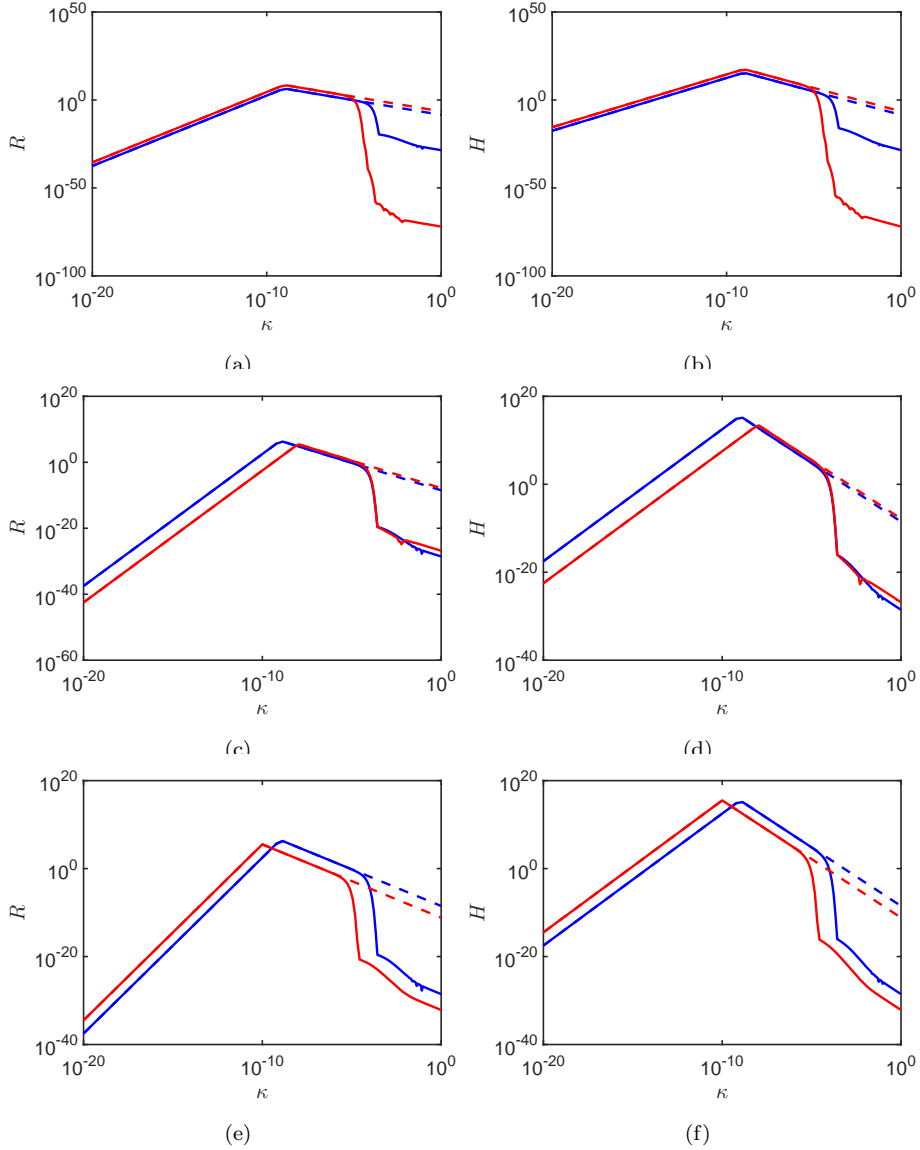


Fig. 1. The spectra versus κ for different parameters of the system. Solid lines are the numerical solution of Eq. (B.2) at EWPT. Dashed lines are the seed spectra at T_{RL} corresponding to Eq. (2.7). Panels (a), (c), and (e): the spectra of the hypermagnetic energy density $R(\kappa)$ in Eq. (B.1). Panels (b), (d), and (f): the spectra of the hypermagnetic helicity density $H(\kappa)$ in Eq. (B.1). Blue lines in panels (a) and (b) correspond to $\tilde{B}_Y^{(0)} = 1.4 \times 10^{-2}$ and red ones to $\tilde{B}_Y^{(0)} = 1.4 \times 10^{-1}$. Additionally $\gamma_* = 10^{-2}$ and $\tilde{k}_{\text{max}} = 10^{-3}$ in panels (a) and (b). Blue lines in panels (c) and (d) correspond to $\gamma_* = 10^{-2}$ and red ones to $\gamma_* = 10^{-3}$. Additionally $\tilde{B}_Y^{(0)} = 1.4 \times 10^{-2}$ and $\tilde{k}_{\text{max}} = 10^{-3}$ in panels (c) and (d). Blue lines in panels (e) and (f) correspond to $\tilde{k}_{\text{max}} = 10^{-3}$ and red ones to $\tilde{k}_{\text{max}} = 10^{-2}$. Additionally $\tilde{B}_Y^{(0)} = 1.4 \times 10^{-2}$ and $\gamma_* = 10^{-2}$ in panels (e) and (f).

8 Maxim Dvornikov

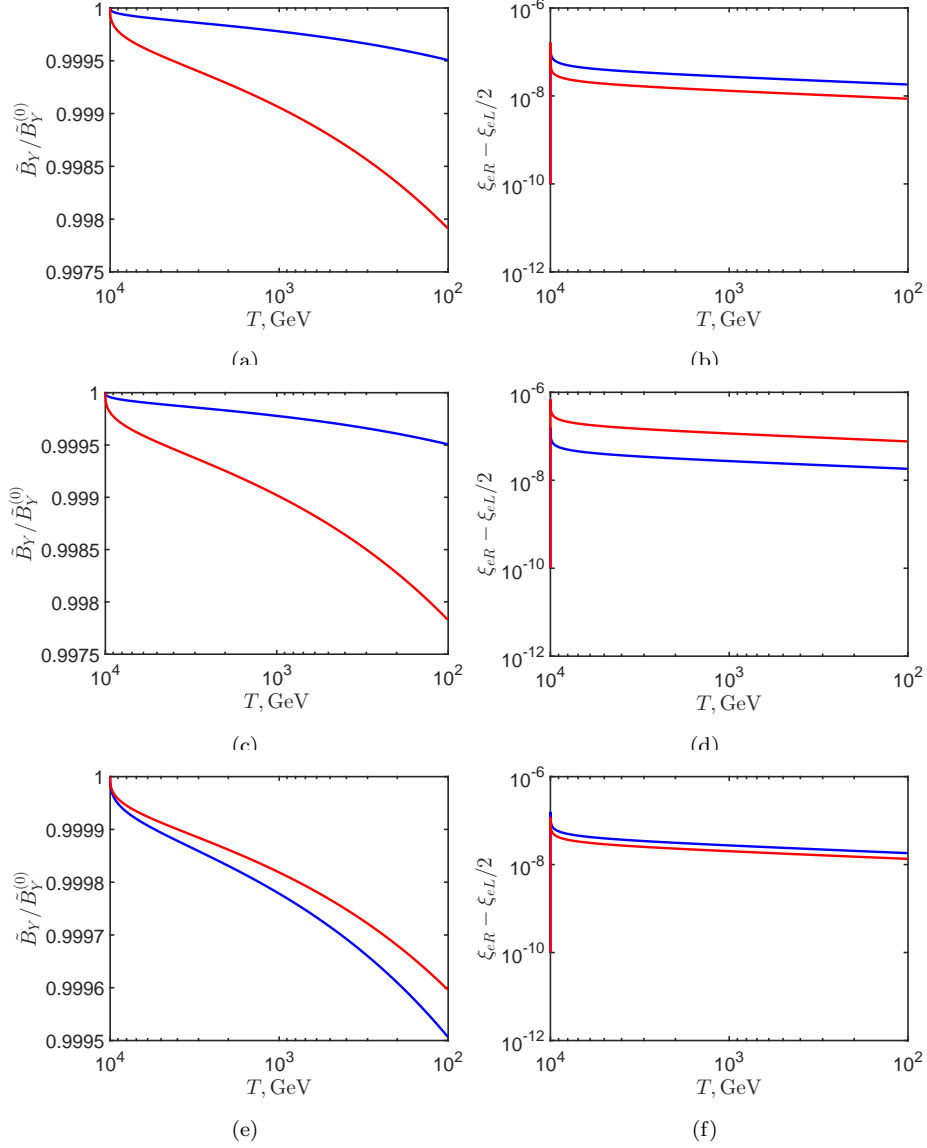


Fig. 2. The strength of HMF \tilde{B}_Y normalized by the seed strength $\tilde{B}_Y^{(0)}$ versus the plasma temperature T is shown in panels (a), (c), and (e) for different parameters of the system. The chiral α -dynamo parameter in Eq. (2.4), $\alpha_Y \propto \xi_{eR} - \xi_{eL}/2$, depending on the plasma temperature T , is depicted in panels (b), (d), and (f) for different parameters of the system. Blue line in panels (a) and (b) correspond to $\tilde{B}_Y^{(0)} = 1.4 \times 10^{-2}$ and red one to $\tilde{B}_Y^{(0)} = 1.4 \times 10^{-1}$. Additionally $\gamma_* = 10^{-2}$ and $\tilde{k}_{\max} = 10^{-3}$ in panels (a) and (b). Blue line in panels (c) and (d) correspond to $\gamma_* = 10^{-2}$ and red one to $\gamma_* = 10^{-3}$. Additionally $\tilde{B}_Y^{(0)} = 1.4 \times 10^{-2}$ and $\tilde{k}_{\max} = 10^{-3}$ in panels (c) and (d). Blue line in panels (e) and (f) correspond to $\tilde{k}_{\max} = 10^{-3}$ and red one to $\tilde{k}_{\max} = 10^{-2}$. Additionally $\tilde{B}_Y^{(0)} = 1.4 \times 10^{-2}$ and $\gamma_* = 10^{-2}$ in panels (e) and (f).

GWs are produced by random HMFs when the energy-momentum tensor of HMFs is accounted for in the right hand side of the Einstein equation which is written down in the expanding universe with the Friedmann–Robertson–Walker (FRW) metric. Using the transverse-traceless gauge and appropriately averaging the expression for the spectrum of the energy density of GWs $\rho_{\text{GW}}^{(c)}(k, \eta)$, one gets that it has form,²³

$$\begin{aligned} \rho_{\text{GW}}^{(c)}(k, \eta) &= \frac{t_{\text{Univ}}^2 G}{4k^3 \pi^2} \eta \int_0^\eta \frac{d\xi}{(\eta_0 + \xi)^2} \int_0^\infty \frac{dq}{q^3} \int_{|k-q|}^{k+q} \frac{dp}{p^3} \\ &\times \{ [4k^2 q^2 + (k^2 + q^2 - p^2)^2] [4k^2 p^2 + (k^2 - q^2 + p^2)^2] \rho_Y^{(c)}(q, \xi) \rho_Y^{(c)}(p, \xi) \\ &+ 4k^2 q^2 p^2 (k^2 + q^2 - p^2)(k^2 - q^2 + p^2) h_Y^{(c)}(q, \xi) h_Y^{(c)}(p, \xi) \}. \end{aligned} \quad (3.1)$$

Here, $\rho_Y^{(c)}(k, \eta)$ and $h_Y^{(c)}(k, \eta)$ are the conformal dimensional spectra of the densities of the HMF energy and the helicity, which are related to the quantities defined in Sec. 2 by $\rho_Y^{(c)}(k, \xi) = \tilde{\mathcal{E}}_{\text{BY}}(\tilde{k}, \tilde{\eta}) T_0^3$ and $h_Y^{(c)}(k, \xi) = \tilde{\mathcal{H}}_{\text{BY}}(\tilde{k}, \tilde{\eta}) T_0^2$, where $T_0 = 2.7$ K is the present temperature of the cosmic microwave background radiation. The dimensional conformal time η and the conformal momentum k in Eq. (3.1) are $\eta = (2t_{\text{Univ}} T_0 / \tilde{M}_{\text{Pl}}) \tilde{\eta}$ and $k = T_0 \tilde{k}$, where $t_{\text{Univ}} = 1.4 \times 10^{10}$ yr is the universe age, as well as $\tilde{\eta}$ and \tilde{k} are defined in Sec. 2. In Eq. (3.1), the parameter $\eta_0 = 2t_{\text{Univ}} T_0 / T_{\text{RL}}$ and $G = M_{\text{Pl}}^{-2}$ is the Newton constant. The total energy density of GWs is calculated on the basis of Eq. (3.1),

$$\rho_{\text{GW}}^{(c)}(\eta) = \int_0^\infty \rho_{\text{GW}}^{(c)}(k, \eta) dk. \quad (3.2)$$

Note that both $\rho_{\text{GW}}^{(c)}(k, \eta)$ and $\rho_{\text{GW}}^{(c)}(\eta)$ in Eqs. (3.1) and (3.2) are conformal.

The total conformal energy density of GWs in Eq. (3.2) is obtained from the time component of the effective energy-momentum tensor, $t_{\mu\nu} = \frac{1}{32\pi G} \langle \partial_\mu h_{\alpha\beta} \partial_\nu h^{\alpha\beta} \rangle$, as $\rho_{\text{GW}}^{(c)} = a^4 t_{00}$. Here $h_{\alpha\beta}$ is the perturbation of the FRW metric and a is the scale factor.

3.1. Results for the GW generation and their observability

In this section, we analyze the generation of relic GWs driven by HMFs relying on the results of numerical simulations in Sec. 2.2. We suppose that $\rho_{\text{GW}}^{(c)}(k, \eta) = 0$ at T_{RL} .

First, basing on the numerical solution of Eq. (2.1) (see also Fig. 1), we show the evolution of $\rho_{\text{GW}}^{(c)}(\eta)$ in the cooling universe in Figs. 3(a), 3(c) and 3(e) normalized by

$$\rho_{\text{GW}}^{(0)} = \frac{\sigma_c^2 \pi^2 t_{\text{Univ}}^2 T_0^8 T_{\text{RL}}^2 G}{576 \alpha'^4 \tilde{M}_{\text{Pl}}^2} = 1.5 \times 10^{-23} \text{ eV} \cdot \text{cm}^{-3}, \quad (3.3)$$

for different parameters of the system. We can see in Figs. 3(a), 3(c) and 3(e) that the energy density of GWs grows despite the HMF strength diminishes; cf. Figs. 2(a),

2(c) and 2(e). As explained in Ref. 23, it results from the cumulative integration over ξ in Eq. (3.1). Note that the behavior of $\rho_{\text{GW}}^{(c)}(\eta)$ qualitatively resembles that found in Ref. 11.

We can see in Fig. 3(a) that the energy density of GWs mainly depends on the seed strength $\tilde{B}_Y^{(0)}$ since the integrand in Eq. (3.1) is quadratic in the HMF spectra. The dependence on γ_\star and \tilde{k}_{max} is not so pronounced. In general, the behavior of $\rho_{\text{GW}}^{(c)}(\eta)$ for the seed spectrum in Eq. 2.7 resembles that for the Kolmogorov seed spectrum, which was studied in Ref. 23.

We obtain the evolution of $\rho_{\text{GW}}^{(c)}(\eta)$ produced by random HMFs accounting for the (H)MHD turbulence, i.e. we replace solving the Navier-Stokes equation for the plasma velocity by the consideration of the effective magnetic diffusion and the α -dynamo parameters in Eq. (2.3). The production of relic GWs by fluctuating magnetic fields in the chiral plasma was recently studied in Ref. 11, where the full set of the MHD equations was solved numerically. The behavior of the total energy density of GWs, found in Ref. 11, is qualitatively the same as in Figs. 3(a), 3(c), and 3(e). It means that the approximation of the (H)MHD turbulence, applied to a chiral plasma, is valid. This fact was also mentioned in Ref. 23.

However, the current GW telescopes cannot measure the GW energy in all range of frequencies. Instead, they are sensitive to the GW energy density in a certain frequency interval. In particular, we discuss the quantity

$$\Omega(f) = \frac{f \rho_{\text{GW}}(f)}{\rho_{\text{crit}}}, \quad (3.4)$$

where $\rho_{\text{crit}} = 0.53 \times 10^{-5} \text{ GeV} \cdot \text{cm}^{-3}$ is the critical energy density of the universe. The derivation of Eq. (3.4) is given in Appendix C. Since k is the conformal momentum, we can call $f = k/2\pi = 5.6 \times 10^{10} \tilde{k}_{\text{max}} \kappa \text{ Hz}$ as the conformal frequency measured in Hz.

We can suppose that GWs generated by $T = T_{\text{EW}}$ remains unchanged at lower temperatures since HMFs are converted to Maxwell ones. Thus, the spectral density at the present moment is $\rho_{\text{GW}}(f) = \rho_{\text{GW}}^{(c)}(f, \eta_{\text{EW}})/a_{\text{now}}^3 = \rho_{\text{GW}}^{(c)}(f, \eta_{\text{EW}})$ since the present scale factor $a_{\text{now}} = 1$. Using Eqs. (3.1) and (B.1), we rewrite Eq. (3.4) in the form,

$$\begin{aligned} \Omega &= \Omega_0 \frac{\tau_{\text{EW}}}{\kappa^2} \int_0^{\tau_{\text{EW}}} \frac{d\tau'}{(1 + 7.1 \times 10^{-13} \tau' / \tilde{k}_{\text{max}}^2)^2} \\ &\times \iint_{S(\kappa)} \frac{dv d\varpi}{v^3 \varpi^3} \\ &\times \{ [4\kappa^2 v^2 + (\kappa^2 + v^2 - \varpi^2)^2] [4\kappa^2 \varpi^2 + (\kappa^2 - v^2 + \varpi^2)^2] R(v, \tau') R(\varpi, \tau') \\ &+ 16\kappa^2 v^2 \varpi^2 (\kappa^2 + v^2 - \varpi^2) (\kappa^2 - v^2 + \varpi^2) H(v, \tau') H(\varpi, \tau') \}, \end{aligned} \quad (3.5)$$

where

$$\Omega_0 = \frac{\sigma_c^2 \pi^2 t_{\text{Univ}}^2 T_0^8 T_{\text{RL}}^2 G}{576 \alpha^4 \tilde{M}_{\text{Pl}}^2 \rho_{\text{crit}}} = 1.6 \times 10^{-24}. \quad (3.6)$$

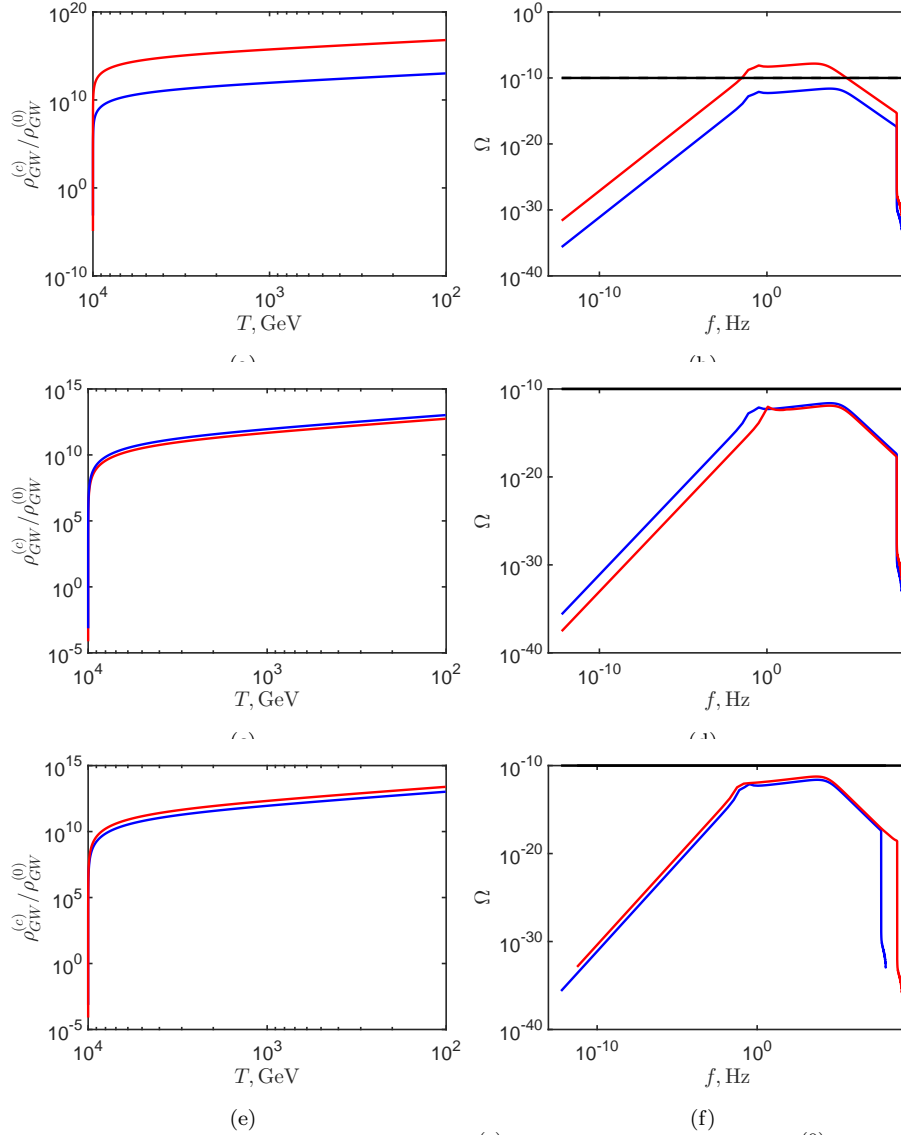


Fig. 3. The conformal energy density of GWs $\rho_{\text{GW}}^{(c)}$ in Eq. (3.2) normalized by $\rho_{\text{GW}}^{(0)}$ in Eq. (3.3) versus the plasma temperature T is shown in panels (a), (c), and (e) for different parameters of the system. The spectral energy density of GWs in Eq. (3.5), depending on the conformal frequency f , is depicted in panels (b), (d), and (f) for different parameters of the system. In panels (b), (d), and (f), by solid black line, we show the observational constraint on Ω , $\Omega_{\text{obs}} \sim 10^{-10}$, established in Ref. 31. Blue line in panels (a) and (b) correspond to $\tilde{B}_Y^{(0)} = 1.4 \times 10^{-2}$ and red one to $\tilde{B}_Y^{(0)} = 1.4 \times 10^{-1}$. Additionally $\gamma_* = 10^{-2}$ and $\tilde{k}_{\text{max}} = 10^{-3}$ in panels (a) and (b). Blue line in panels (c) and (d) correspond to $\gamma_* = 10^{-2}$ and red one to $\gamma_* = 10^{-3}$. Additionally $\tilde{B}_Y^{(0)} = 1.4 \times 10^{-2}$ and $\tilde{k}_{\text{max}} = 10^{-3}$ in panels (c) and (d). Blue line in panels (e) and (f) correspond to $\tilde{k}_{\text{max}} = 10^{-3}$ and red one to $\tilde{k}_{\text{max}} = 10^{-2}$. Additionally $\tilde{B}_Y^{(0)} = 1.4 \times 10^{-2}$ and $\gamma_* = 10^{-2}$ in panels (e) and (f).

Here, $S(\kappa)$ is the polygon integration domain in the $(v\varpi)$ -plane.

We show Ω versus f in Figs. 3(b), 3(d), and 3(f) for different parameters of the system. We can see that Ω reaches its maximal values in a plateau which spans from \sim Hz to \sim kHz. It matches the frequency range probed in Ref. 31 in the search of a stochastic GW background. The observational upper bound established in Ref. 31 is $\Omega_{\text{obs}} \sim 10^{-10}$, which is also depicted in Figs. 3(b), 3(d), and 3(f). For the convenience, we summarize the parameters of the plateaus in Table 1.

Table 1. The frequency range and the values of Ω corresponding to the plateaus in Figs. 3(b), 3(d), and 3(f).

Figure	Type of line	f_{plat} (f_{max})	Ω_{plat} (Ω_{max})
Fig. 3(b) ($\gamma_\star = 10^{-2}$ and $\tilde{k}_{\text{max}} = 10^{-3}$)	Blue line ($\tilde{B}_Y^{(0)} = 1.4 \times 10^{-2}$)	$0.3 \text{ Hz} < f_{\text{plat}} < 5.9 \text{ kHz}$	$7.9 \times 10^{-13} < \Omega_{\text{plat}} < 2.4 \times 10^{-12}$
	Red line ($\tilde{B}_Y^{(0)} = 1.4 \times 10^{-1}$)	$0.3 \text{ Hz} < f_{\text{plat}} < 631 \text{ Hz}$	$7.8 \times 10^{-9} < \Omega_{\text{plat}} < 1.5 \times 10^{-8}$
Fig. 3(d) ($\tilde{B}_Y^{(0)} = 1.4 \times 10^{-2}$ and $\tilde{k}_{\text{max}} = 10^{-3}$)	Blue line ($\gamma_\star = 10^{-2}$)	$0.3 \text{ Hz} < f_{\text{plat}} < 5.9 \text{ kHz}$	$7.9 \times 10^{-13} < \Omega_{\text{plat}} < 2.4 \times 10^{-12}$
	Red line ($\gamma_\star = 10^{-3}$)	$1.1 \text{ Hz} < f_{\text{plat}} < 5.9 \text{ kHz}$	$9.5 \times 10^{-13} < \Omega_{\text{plat}} < 1.3 \times 10^{-12}$
Fig. 3(f) ($\tilde{B}_Y^{(0)} = 1.4 \times 10^{-2}$ and $\gamma_\star = 10^{-2}$)	Blue line ($\tilde{k}_{\text{max}} = 10^{-3}$)	$0.3 \text{ Hz} < f_{\text{plat}} < 5.9 \text{ kHz}$	$7.9 \times 10^{-13} < \Omega_{\text{plat}} < 2.4 \times 10^{-12}$
	Red line ($\tilde{k}_{\text{max}} = 10^{-2}$)	$f_{\text{max}} = 4.6 \text{ kHz}$	$\Omega_{\text{max}} = 5.7 \times 10^{-12}$

The plateau in Figs. 3(b), 3(d), and 3(f) is defined as the part of a curve between two first maxima in Ω if the difference between them is about one order of magnitude. If the difference between maxima is greater, we deal with just a single maximum, as in the last row in Table 1.

We can see that only in the case corresponding to $\gamma_\star = 10^{-2}$, $\tilde{k}_{\text{max}} = 10^{-3}$, and $\tilde{B}_Y^{(0)} = 1.4 \times 10^{-1}$, shown in Fig. 3(b) by the red line (see also the second row in Table 1), Ω , predicted in our model, exceeds Ω_{obs} . Thus, we can put the constraint on $\tilde{B}_Y^{(0)}$, $\tilde{B}_Y^{(0)} \lesssim 10^{-1}$, or $B_Y^{(0)} = T_{\text{RL}}^2 \tilde{B}_Y^{(0)} \lesssim 5 \times 10^{26} \text{ G}$. Such a HMF, while evolving down to the big bang nucleosynthesis (BBN) temperature $T_{\text{BBN}} = 0.1 \text{ MeV}$, has the strength $B(T = T_{\text{BBN}}) = T_{\text{BBN}}^2 \tilde{B}_Y^{(0)} = 5 \times 10^{10} \text{ G}$. This constraint is in agreement with the BBN upper bound $B_{\text{BBN}} = 10^{11} \text{ G}$ obtained in Ref. 32. Other parameters of the system do not violate the observational constraints on Ω .

4. Flavor oscillations of SN neutrinos in relic GWs

In this section, we examine how relic GWs produced by HMFs, described in Sec. 3, influence flavor oscillations of SN neutrinos. The interaction between stochastic GWs and neutrinos, as well as neutrino flavor oscillations were studied in Refs. 15, 16, 17.

We consider the system of three mixed massive flavor neutrinos $\lambda = \nu_e, \nu_\mu, \nu_\tau$ interacting with stochastic GWs. The probability to detect a certain neutrino flavor $\lambda = \nu_e, \nu_\mu, \nu_\tau$ in a neutrino beam, which travels the distance x between the emission

and the detection points, was found in Ref. 17,

$$P_\lambda^{(g)}(x) = \sum_\sigma P_\sigma(0) \left[\sum_a |U_{\lambda a}|^2 |U_{\sigma a}|^2 + 2\text{Re} \sum_{a>b} U_{\lambda a} U_{\lambda b}^* U_{\sigma a}^* U_{\sigma b} \exp(-i\varphi_{ab}x) g_{ab} \right], \quad (4.1)$$

where $P_\sigma(0)$ are the emission probabilities, which satisfy $\sum_\sigma P_\sigma(0) = 1$, $(U_{\lambda a})$ is the mixing matrix between mass and flavor bases, $\varphi_{ab} = \frac{\Delta m_{ab}^2}{2E}$ are the phases of neutrino vacuum oscillations, $\Delta m_{ab}^2 = m_a^2 - m_b^2$, with $a, b = 1, 2, 3$, are the differences of the masses squared of the neutrino mass eigenstates, E is the mean neutrino energy, $g_{ab}(x) = \exp[-\varphi_{ab}^2 \int_0^x g(t) dt]$, $g(t) = \frac{3}{128} \int_0^t dt_1 (\langle h_+(t) h_+(t_1) \rangle + \langle h_\times(t) h_\times(t_1) \rangle)$, and $h_{+, \times}$ are the random amplitudes of ‘plus’ and ‘times’ polarizations of the GW background. The details of the derivation of Eq. (4.1) are also given in Appendix D. The observed neutrino fluxes are $F_\lambda \propto P_\lambda^{(g)}$.

If we consider SN neutrinos, basing on Eq. (4.1), one gets that only solar oscillations channel contributes to the probabilities. It is convenient to subtract the effect of neutrino vacuum oscillations from the total probabilities by considering $\Delta P_\lambda = P_\lambda^{(g)} - P_\lambda^{(\text{vac})}$. Finally, we can rewrite ΔP_λ in the form,¹⁷

$$\Delta P_\lambda(x) = 2 \left[\text{Re} [U_{\lambda 2} U_{\lambda 1}^* U_{e 2}^* U_{e 1}] \cos\left(2\pi \frac{x}{L_{21}}\right) + \text{Im} [U_{\lambda 2} U_{\lambda 1}^* U_{e 2}^* U_{e 1}] \sin\left(2\pi \frac{x}{L_{21}}\right) \right] \times [1 - \exp(-\Gamma_\nu)], \quad \Gamma_\nu = \frac{4\pi^2}{L_{21}^2} \int_0^x g(t) dt. \quad (4.2)$$

where $L_{21} = \frac{4\pi E}{\Delta m_{21}^2}$ is the oscillations length in vacuum for the solar channel. We should evaluate the parameter Γ_ν for the GW background considered in Sec. 3. The contribution of GWs would be sizable if $\Gamma_\nu > 1$.

We can rewrite the correlators of the amplitudes using the spectral density $S(\omega)$ as

$$\langle h_+(t) h_+(t_1) \rangle + \langle h_\times(t) h_\times(t_1) \rangle = \int_0^\infty d\omega S(\omega) \cos[\omega(t - t_1)]. \quad (4.3)$$

Thus,

$$g(t) = \frac{3}{128} \int_0^\infty \frac{d\omega}{\omega} \sin(\omega t) S(\omega), \quad (4.4)$$

and

$$\Gamma_\nu(x) = \frac{6\pi^3 G}{L_{21}^2} \int_0^\infty \frac{d\omega}{\omega^4} \sin^2(\omega x/2) \rho_{\text{GW}}(\omega), \quad (4.5)$$

since $k = \omega$ for a GW wave. Hence, the spectrum of the energy density is related to $S(\omega)$ by $\rho_{\text{GW}}(k = \omega) = \omega^2 S(\omega)/32\pi G$. As a rule, the distance between the Earth, where we observe the neutrino flux, and SN is great. Thus, we should consider Eq. (4.5) in the limit $x \rightarrow \infty$,

$$\Gamma_\oplus(x) = \frac{3\pi^4 G}{4L_{21}^2} x \lim_{\omega \rightarrow 0} \frac{\rho_{\text{GW}}(\omega)}{\omega^2}, \quad (4.6)$$

where take into account the δ -function definition, $\delta(\alpha) = \lim_{x \rightarrow \infty} \frac{\sin^2(\alpha x)}{\pi x \alpha^2}$.

The spectrum of the energy density of GWs is given in Eq. (3.1). We suppose that there is no GW production after EWPT, i.e. the conformal spectrum is constant after EWPT. Thus we should put $\eta = \eta_{\text{EW}}$ in Eq. (3.1). Considering the limit $k \rightarrow 0$ and taking that $\rho_{\text{GW}}(\omega) = \rho_{\text{GW}}^{(c)}(k, \eta_{\text{EW}})$ since we study the neutrino propagation and oscillations at the present time, one gets that

$$\rho_{\text{GW}}^{(c)}(k, \eta_{\text{EW}}) \rightarrow k^2 \frac{8t_{\text{Univ}}^2 G}{\pi^2} \eta_{\text{EW}} \int_0^{\eta_{\text{EW}}} \frac{d\xi}{(\eta_0 + \xi)^2} \int_0^{k_{\text{max}}} \frac{dp}{p^2} \left[\rho_{\text{V}}^{(c)}(p, \xi) \right]^2. \quad (4.7)$$

Finally, using Eq. (B.1), we rewrite Eq. (4.6) as

$$\Gamma_{\oplus}(x) = \left(\frac{x}{L} \right) \Gamma_0, \quad \Gamma_0 = N I_{\nu}, \quad (4.8)$$

where

$$N = \frac{\sigma_c \pi^6 t_{\text{Univ}}^2 G^2 T_0^5 T_{\text{RL}} L}{6\alpha^4 M_{\text{Pl}} L_{21}^2 \tilde{k}_{\text{max}}^3} = \frac{1.6 \times 10^{-76}}{\tilde{k}_{\text{max}}^3},$$

$$I_{\nu} = \int_0^{\tau_{\text{EW}}} \frac{\tau_{\text{EW}} d\tau}{(1 + 7.1 \times 10^{-13} \tau / \tilde{k}_{\text{max}}^2)^2} \int_0^1 \frac{d\kappa}{\kappa^2} R^2(\kappa, \tau). \quad (4.9)$$

Here we normalize the neutrino propagation distance on the typical galaxy size $L = 10$ kpc. The integral in Eq. (4.9) is computed using the results of Sec. 2.2 (see Fig. 1).

We show the parameter Γ_0 versus \tilde{k}_{max} for different $\tilde{B}_Y^{(0)}$ and γ_* in Fig. 4. One can see that $\Gamma_0 \ll 1$ for the reasonable values of all parameters. Even if we consider an extragalactic SN and take $x \sim 1$ Gpc, Γ_{\oplus} still remains quite small. Thus, using Eq. (4.2), one gets that $\Delta P_{\lambda} \ll 1$.

It means that the GW background generated by HMFs does not influence flavor oscillations of SN neutrinos unlike stochastic GWs produced by merging supermassive black holes (SMBHs), which were studied in Ref. 17. Such a difference between the results is because of the fact that Ω in case of stochastic GWs generated by coalescing SMBHs is nonzero for $f \geq f_{\text{min}} \neq 0$. In our case, $\rho_{\text{GW}}(f) \propto f^2$ for small frequencies, i.e. $f_{\text{min}} = 0$.

5. BAU caused by the lepton asymmetries

The self-consistent evolution of HMFs and the asymmetries of leptons and Higgs bosons in Eq. (2.1) give rise to not only relic GWs. If we focus on the $\xi_{e,R,L}$ evolution, we can predict the generated BAU at EWPT. We studied this problem in Ref. 22 basing on the Kolmogorov spectrum of seed HMFs. Now we reexamine the issue of the BAU generation in HMFs using a more realistic seed spectrum in Eq. (2.5).

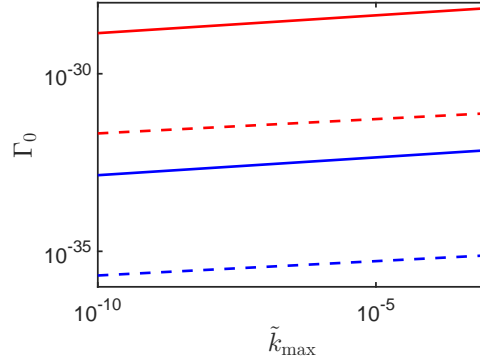


Fig. 4. The parameter Γ_0 in Eq. (4.8) versus \tilde{k}_{\max} for different values of $\tilde{B}_Y^{(0)}$ and γ_* . Red lines correspond to $\tilde{B}_Y^{(0)} = 1.4 \times 10^{-2}$ and blue ones to $\tilde{B}_Y^{(0)} = 1.4 \times 10^{-3}$. Solid lines are plotted for $\gamma_* = 10^2$ and dashed ones for $\gamma_* = 10^3$.

Given the asymmetries of right and left leptons $\xi_{eR,L}$, BAU has the form,²²

$$\begin{aligned} \text{BAU}(\tilde{\eta}) &= \frac{n_B - n_{\bar{B}}}{s} = 5.3 \times 10^{-3} \int_0^{\tilde{\eta}} d\tilde{\eta}' \\ &\times \left\{ \frac{d\xi_{eR}(\tilde{\eta}')}{d\tilde{\eta}'} + \Gamma(\tilde{\eta}') [\xi_{eR}(\tilde{\eta}') - \xi_{eL}(\tilde{\eta}')] \right\} - \frac{6 \times 10^7}{\tilde{\eta}_{\text{EW}}} \int_0^{\tilde{\eta}} \xi_{eL}(\tilde{\eta}') d\tilde{\eta}', \end{aligned} \quad (5.1)$$

where $n_{B,\bar{B}}$ are number densities of baryons and antibaryons, and s is the entropy density. Equation (5.1) implies that BAU = 0 at $T = T_{\text{RL}}$.

We show the evolution of BAU in the universe cooling from T_{RL} down to T_{EW} for different γ_* and $\xi_{eR}^{(0)}$ in Fig. 5. For fixed $\tilde{B}_Y^{(0)}$ and γ_* , BAU does not significantly depend on \tilde{k}_{\max} . That is why we use the constant value $\tilde{k}_{\max} = 10^{-3}$ in our simulations. If $\tilde{B}_Y^{(0)} > 1.4 \times 10^{-6}$, BAU exceeds the observed value $\text{BAU}_{\text{obs}} \sim 10^{-10}$. Thus, we do not consider quite strong seed HMFs as we made in Secs. 2.2 and 3.1.

In Figs. 5(a) and 5(b), we also examine the dependence of BAU on the initial right electrons asymmetry. When $\xi_{eR}^{(0)} = 10^{-10}$, we get that $\text{BAU}_{\text{obs}} \sim 10^{-10}$ at EWPT. The enhancement of $\xi_{eR}^{(0)}$ results in BAU which exceeds the observed value; cf Fig. 5(b). The excessive BAU in Fig. 5(b) cannot be reduced by varying other parameters of the system. Thus, the generated BAU is almost completely defined by the initial right electrons asymmetry.

One can see in Fig. 5(a) that we reach the observed BAU at $T = T_{\text{EW}} = 10^2$ GeV if $\tilde{B}_Y^{(0)} = 1.4 \times 10^{-6}$. This result corresponds to the seed spectrum in Eq. (2.5). We obtained in Ref. 22 that $\text{BAU}_{\text{obs}} \sim 10^{-10}$ can be achieved at significantly stronger seed HMFs with $\tilde{B}_Y^{(0)} \sim 1.4 \times (10^{-2} \div 10^{-1})$. However, those HMFs in Ref. 22 corresponded to the seed Kolmogorov spectrum. It means that the consideration of BAU as a consequence of the evolution of HMFs and the asymmetries in Eq. (2.1) imposes a stronger constraint on $\tilde{B}_Y^{(0)}$ in comparison with the relic GWs background

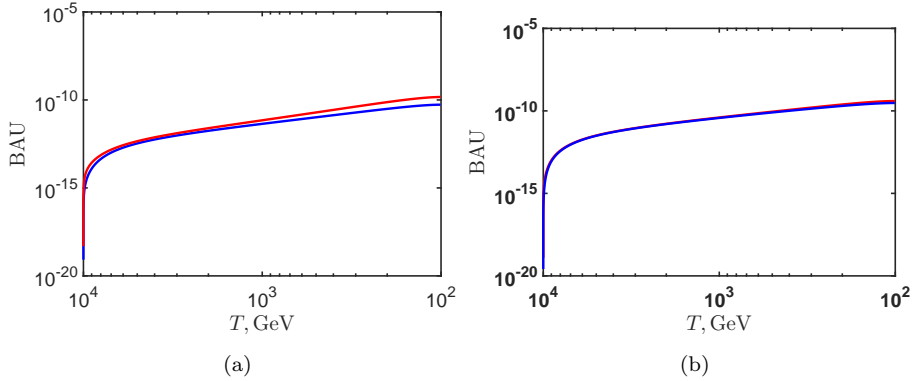


Fig. 5. The evolution of BAU based on the numerical solution of Eq. (2.1) corresponding to the initial condition in Sec. 2.1. We take that $\tilde{B}_Y^{(0)} = 1.4 \times 10^{-6}$ and $\tilde{k}_{\max} = 10^{-3}$. Blue lines correspond to $\gamma_* = 10^{-2}$ and red ones to $\gamma_* = 10^{-3}$. (a) $\xi_{eR}^{(0)} = 10^{-10}$; (b) $\xi_{eR}^{(0)} = 10^{-9}$.

studied in Sec. 3.1.

6. Conclusion

In the present work, we have studied the evolution of random HMFs in the early universe cooling down from $T_{\text{RL}} = 10 \text{ TeV}$ to $T_{\text{EW}} = 100 \text{ GeV}$. The evolution of HMFs is driven by the analog of the CME and accounts for the (H)MHD turbulence. The analog of the CME involves the asymmetries, proportional to the chiral imbalances, of right and left leptons. The initial temperature $T_{\text{RL}} = 10 \text{ TeV}$ is chosen so that the contributions of the asymmetries in Eq. (2.1) are self-consistent, i.e. left leptons start to be produced. The final temperature $T_{\text{EW}} = 100 \text{ GeV}$ corresponds to EWPT when particles acquire masses and the chiral approximation is no longer valid.

The (H)MHD turbulence implies the dominant role of the Lorentz force in the Navier-Stokes equation. In Appendix A, we have rederived the turbulent terms in the kinetic equations for the spectra of the magnetic energy and the magnetic helicity (see Eqs. (2.3) and (A.10)). We have corrected the form of the α -dynamo parameter used in Refs. 22, 23, 29. Now, our results are consistent with Ref. 28. However, as found in Sec. 2.2 and claimed in Refs. 22, 23, the evolution of HMFs is dominated by the diffusion rather than the α -dynamo term.

The main advance of the present work in comparison with Refs. 22, 23 is the consideration of a more realistic seed spectrum of HMFs which is Batchelor at small momenta and Kolmogorov at great ones. The necessity of the vanishing spectrum at great length scales, comparable with the horizon size, was mentioned in Ref. 30. Now, we do not have to consider the minimal momentum. However, we should take into account the border momentum \tilde{k}_* (see Eq. (2.5)), or γ_* , which is a new free parameter in the system.

In Sec. 2.1, we have formulated the initial condition for Eq. (2.1) and numer-

ically solved it in Sec. 2.2. The system in Eq. (2.1) has been represented in the form convenient for numerical simulations in Appendix B. We have obtained the behavior of the spectra of the magnetic energy and the magnetic helicity, as well as the evolution the HMFs strength and the α -dynamo parameter; cf. Figs. 1 and 2. Qualitatively, the evolution of these parameters resembles that found in Refs. 22, 23.

We have studied the various phenomena affected by HMFs. First, in Sec. 3, we have considered the production of relic GWs by random HMFs. For this purpose, we have used the formalism developed in Ref. 23. We have tracked the evolution of the energy density of GWs from T_{RL} down to EWPT in Sec. 3.1. We have also discussed the observability of the predicted GW background by the current GW detectors. The maximum of the spectral density of the predicted GW signal is in the range from \sim Hz to \sim kHz. It coincides with the sensitivity of the LIGO-Virgo-KAGRA collaborations.³¹ Thus, in Sec. 3.1, we could establish the constraint on the strength of HMF which is $\tilde{B}_Y^{(0)} \lesssim 10^{-1}$ or $B_Y^{(0)} < 5 \times 10^{26}$ G. The obtained upper limit is consistent with the BBN constraint on the magnetic field strength derived in Ref. 32.

In Sec. 4, we have discussed flavor oscillations of SN neutrinos in relic GWs predicted in our model. We have used the formalism for the description of neutrino flavor oscillations in GWs developed in Refs. 15, 16, 17. Some of the issues of this formalism were clarified in Appendix D. We have analyzed whether the neutrino interaction with GWs can modify the observed fluxes of SN neutrinos. We have obtained that the contribution of GWs to the fluxes is rather small for realistic SN neutrinos.

Finally, in Sec. 5, we have calculated BAU which is generated in the wake of the evolution of the asymmetries of right and left leptons. For this purpose, we have applied the technique developed in Ref. 22. We have obtained that, in order not to exceed the observed $\text{BAU}_{\text{obs}} \sim 10^{-10}$, we should constrain the strength of the seed HMF by $\tilde{B}_Y^{(0)} \lesssim 10^{-6}$, or $B_Y^{(0)} < 5 \times 10^{20}$ G. This upper limit is stronger than that derived in Sec. 3.1 basing on the observability of relic GWs. Moreover, it is also stronger than the result of Ref. 22, where analogous problem was studied and we used the Kolmogorov seed spectrum. The upper bound on the seed HMF derived from the consideration of BAU is consistent with the result of Ref. 33.

Generally, the α -dynamo mechanism used in our work to drive the evolution of HMFs requires a nonzero seed field $B_Y^{(0)}$. We do not explain origin of $B_Y^{(0)}$. Only constraints on the seed field are established. Nevertheless, there are models for the production of a seed field in the inflationary epoch (see, e.g., Ref. 34). This inflation based HMF evolves in the cooling universe down to $T_{\text{RL}} = 10$ TeV leading to $B_Y^{(0)}$ used in our work. Quantum fluctuations during the inflation can be of the tensor type and lead to the production of GWs.³⁵ In particular, we mention the generation of relic GWs in (pre-)inflationary times within the modifications of the General Relativity which was studied in Refs. 36, 37, 38. Various models for the

production of primordial GWs in modified gravity theories, including the analysis of the GW spectra generated, are reviewed in Ref. 39. There are attempts to probe such GWs.^{40,41} In our work, we do not take into account primordial GWs produced during the inflation. The only possible impact of physics processes in the inflationary epoch on our results is the generation of a seed HMF.

Acknowledgments

I am thankful to V. B. Semikoz and M. E. Shaposhnikov for the communications.

Appendix A. Contribution of the MHD turbulence to the coefficients in the kinetic equations

In this appendix, we reexamine the contribution of random magnetic fields to the kinetic equations for the magnetic energy and the helicity within the approximation of the MHD turbulence. This problem was studied in Refs. 28, 29 leading to the contradictory results. We omit the subscript ‘Y’ for brevity dealing with Maxwell magnetic fields. The generalization of the results to HMFs is straightforward.

We shall keep the notations similar to Refs. 28, 29 as close as possible. First, we fix the Fourier transform as $\mathbf{B}(\mathbf{k}) = \int d^3x e^{i\mathbf{k}\cdot\mathbf{x}} \mathbf{B}(\mathbf{x})$. Since we study random fields, we take that the equal times correlator of the magnetic fields strengths reads^{28,29}

$$\langle B_j(\mathbf{k}, t) B_i(\mathbf{p}, t) \rangle = \frac{(2\pi)^3}{2} \delta(\mathbf{k} + \mathbf{p}) \left[(\delta_{ji} - \hat{k}_j \hat{k}_i) S(k, t) + i \varepsilon_{jin} \hat{k}_n A(k, t) \right], \quad (\text{A.1})$$

where $\hat{\mathbf{k}} = \mathbf{k}/k$, $k = |\mathbf{k}|$, and

$$S(k, t) = \frac{4\pi^2 \rho(k, t)}{k^2}, \quad A(k, t) = \frac{2\pi^2 h(k, t)}{k}, \quad (\text{A.2})$$

are related to the spectra of the densities of the magnetic energy $\rho(k, t)$ and the helicity $h(k, t)$. The densities of energy and helicity have the form, $B^2/2 = \int dk \rho(k, t)$ and $h \equiv \int d^3x (\mathbf{A}\mathbf{B})/V = \int dk h(k, t)$. Here, we are in frames of the mean field approximation.

We use the MHD approximation,⁴² in which the plasma velocity is $\mathbf{v} = \frac{\tau_d}{P + \rho} (\mathbf{J} \times \mathbf{B})$, where τ_d is the phenomenological drag time, \mathbf{J} is the electric current, P is the plasma pressure, ρ is the energy density of matter. Substituting such velocity to the induction equation, $\dot{\mathbf{B}} = \nabla \times (\mathbf{v} \times \mathbf{B}) + \eta_m \Delta \mathbf{B}$, where η_m is the magnetic diffusion coefficient, and making the Fourier transform, we derive the evolution equation in the form,^{28,29}

$$\dot{B}_j(\mathbf{k}) = -\eta_m k^2 B_j(\mathbf{k}) + \Xi_j(\mathbf{k}), \quad (\text{A.3})$$

where

$$\begin{aligned} \Xi_j(\mathbf{k}) = & \frac{\tau_d}{P + \rho} \int \frac{d^3l}{(2\pi)^3} \frac{d^3q}{(2\pi)^3} \varepsilon_{jtk} k_t q_r B_s(\mathbf{q}) \\ & \times [\varepsilon_{krs} B_n(\mathbf{l} - \mathbf{q}) B_n(\mathbf{k} - \mathbf{l}) - \varepsilon_{rms} B_k(\mathbf{k} - \mathbf{l}) B_m(\mathbf{l} - \mathbf{q})]. \end{aligned} \quad (\text{A.4})$$

We differentiate Eq. (A.1) by time and use Eq. (A.3),

$$\begin{aligned}
 \left\langle \dot{B}_j(\mathbf{k}, t) B_i(\mathbf{p}, t) + B_j(\mathbf{k}, t) \dot{B}_i(\mathbf{p}, t) \right\rangle &= \frac{(2\pi)^3}{2} \delta(\mathbf{k} + \mathbf{p}) \\
 &\times \left[\left(\delta_{ji} - \hat{k}_j \hat{k}_i \right) \dot{S}(k, t) + i \varepsilon_{jin} \hat{k}_n \dot{A}(k, t) \right] \\
 &= -\eta_m k^2 (2\pi)^3 \delta(\mathbf{k} + \mathbf{p}) \left[\left(\delta_{ji} - \hat{k}_j \hat{k}_i \right) S(k, t) + i \varepsilon_{jin} \hat{k}_n A(k, t) \right] \\
 &\quad + \langle B_i(\mathbf{p}, t) \Xi_j(\mathbf{k}, t) + B_j(\mathbf{k}, t) \Xi_i(\mathbf{p}, t) \rangle. \quad (\text{A.5})
 \end{aligned}$$

Multiplying Eq. (A.5) by δ_{ij} and $i \varepsilon_{ijn} \hat{k}_n$, we get the following equations for S and A :

$$\begin{aligned}
 \delta(\mathbf{k} + \mathbf{p}) \left[\dot{S}(k, t) + 2\eta_m k^2 S(k, t) \right] &= \frac{1}{(2\pi)^3} \langle B_i(\mathbf{p}, t) \Xi_i(\mathbf{k}, t) + B_i(\mathbf{k}, t) \Xi_i(\mathbf{p}, t) \rangle, \\
 \delta(\mathbf{k} + \mathbf{p}) \left[\dot{A}(k, t) + 2\eta_m k^2 A(k, t) \right] &= \frac{i \varepsilon_{ijn} \hat{k}_n}{(2\pi)^3} \langle B_i(\mathbf{p}, t) \Xi_j(\mathbf{k}, t) + B_j(\mathbf{k}, t) \Xi_i(\mathbf{p}, t) \rangle.
 \end{aligned} \quad (\text{A.6})$$

The quantity $\langle B_i(\mathbf{p}, t) \Xi_j(\mathbf{k}, t) + B_j(\mathbf{k}, t) \Xi_i(\mathbf{p}, t) \rangle$ contains four-point correlators which can be expressed through two-point ones, as prescribed in Refs. 28, 29.

Using Eq. (A.4), we obtain that

$$\begin{aligned}
 \langle B_i(\mathbf{p}) \Xi_j(\mathbf{k}) + B_j(\mathbf{k}) \Xi_i(\mathbf{p}) \rangle &= \delta(\mathbf{k} + \mathbf{p}) \frac{\tau_d}{4(P + \rho)} \int d^3 q \left[2k_t k_r \varepsilon_{krs} S(q) \right. \\
 &\times \left\{ \varepsilon_{jtk} \left[\left(\delta_{is} - \hat{k}_i \hat{k}_s \right) S(k) - i \varepsilon_{isl} \hat{k}_l A(k) \right] + \varepsilon_{itk} \left[\left(\delta_{js} - \hat{k}_j \hat{k}_s \right) S(k) + i \varepsilon_{jsl} \hat{k}_l A(k) \right] \right\} \\
 &+ 2k_t q_r \varepsilon_{krs} \left[\left(\delta_{sn} - \hat{q}_s \hat{q}_n \right) S(q) + i \varepsilon_{snl} \hat{q}_l A(q) \right] \\
 &\times \left\{ \varepsilon_{jtk} \left[\left(\delta_{in} - \hat{k}_i \hat{k}_n \right) S(k) - i \varepsilon_{inl} \hat{k}_l A(k) \right] - \varepsilon_{itk} \left[\left(\delta_{jn} - \hat{k}_j \hat{k}_n \right) S(k) + i \varepsilon_{jnl} \hat{k}_l A(k) \right] \right\} \\
 &- k_t k_r \varepsilon_{rms} \left[\left(\delta_{km} - \hat{q}_k \hat{q}_m \right) S(q) - i \varepsilon_{kml} \hat{q}_l A(q) \right] \\
 &\times \left\{ \varepsilon_{jtk} \left[\left(\delta_{is} - \hat{k}_i \hat{k}_s \right) S(k) - i \varepsilon_{isl} \hat{k}_l A(k) \right] + \varepsilon_{itk} \left[\left(\delta_{js} - \hat{k}_j \hat{k}_s \right) S(k) + i \varepsilon_{jsl} \hat{k}_l A(k) \right] \right\} \\
 &- k_t q_r \varepsilon_{rms} \left[\left(\delta_{sm} - \hat{q}_s \hat{q}_m \right) S(q) + i \varepsilon_{sml} \hat{q}_l A(q) \right] \\
 &\times \left\{ \varepsilon_{jtk} \left[\left(\delta_{ik} - \hat{k}_i \hat{k}_k \right) S(k) - i \varepsilon_{ikl} \hat{k}_l A(k) \right] - \varepsilon_{itk} \left[\left(\delta_{jk} - \hat{k}_j \hat{k}_k \right) S(k) + i \varepsilon_{jkl} \hat{k}_l A(k) \right] \right\} \\
 &- k_t q_r \varepsilon_{rms} \left[\left(\delta_{sk} - \hat{q}_s \hat{q}_k \right) S(q) + i \varepsilon_{skl} \hat{q}_l A(q) \right] \\
 &\times \left\{ \varepsilon_{jtk} \left[\left(\delta_{im} - \hat{k}_i \hat{k}_m \right) S(k) - i \varepsilon_{iml} \hat{k}_l A(k) \right] - \varepsilon_{itk} \left[\left(\delta_{jm} - \hat{k}_j \hat{k}_m \right) S(k) + i \varepsilon_{jml} \hat{k}_l A(k) \right] \right\}.
 \end{aligned} \quad (\text{A.7})$$

Equation (A.7) is written down in such a form intentionally. It allows one to separate symmetric and antisymmetric combinations in the indexes ij which enter to

20 *Maxim Dvornikov*

Eq. (A.6). Basing on Eq. (A.7), we rewrite Eq. (A.6) in the form,

$$\begin{aligned} \dot{S}(k, t) + 2\eta_m k^2 S(k, t) &= \frac{\tau_d}{2(P + \rho)} \left\{ -k^2 S(k, t) \int \frac{d^3 q}{(2\pi)^3} S(q, t) \left[3 - (\hat{\mathbf{k}}\hat{\mathbf{q}})^2 \right] \right. \\ &\quad \left. + k A(k, t) \int \frac{d^3 q}{(2\pi)^3} q A(q, t) \left[3 - (\hat{\mathbf{k}}\hat{\mathbf{q}})^2 \right] \right\}, \\ \dot{A}(k, t) + 2\eta_m k^2 A(k, t) &= \frac{\tau_d}{2(P + \rho)} \left\{ -k^2 A(k, t) \int \frac{d^3 q}{(2\pi)^3} S(q, t) \left[3 - (\hat{\mathbf{k}}\hat{\mathbf{q}})^2 \right] \right. \\ &\quad \left. + k S(k, t) \int \frac{d^3 q}{(2\pi)^3} q A(q, t) \left[3 - (\hat{\mathbf{k}}\hat{\mathbf{q}})^2 \right] \right\}. \end{aligned} \quad (\text{A.8})$$

Using Eq. (A.2), we express Eq. (A.8) as

$$\begin{aligned} \frac{\partial \rho(k, t)}{\partial t} &= -2\eta_{\text{eff}} k^2 \rho(k, t) + \alpha_{\text{eff}} k^2 h(k, t), \\ \frac{\partial h(k, t)}{\partial t} &= -2\eta_{\text{eff}} k^2 h(k, t) + 4\alpha_{\text{eff}} \rho(k, t), \end{aligned} \quad (\text{A.9})$$

where

$$\eta_{\text{eff}} = \eta_m + \frac{4}{3} \frac{\tau_d}{P + \rho} \int dq \rho(q, t), \quad \alpha_{\text{eff}} = \frac{2}{3} \frac{\tau_d}{P + \rho} \int dq q^2 h(q, t). \quad (\text{A.10})$$

Equations (A.9) and (A.10) coincide with those in Ref. 28.

Appendix B. New variables for the numerical simulation of the HMFs evolution

In the numerical solution of Eq. (2.1), we use the new variables,^{22,23}

$$\begin{aligned} \tilde{\mathcal{E}}_{\text{BY}}(\tilde{k}, \tilde{\eta}) &= \frac{\tilde{k}_{\text{max}} \pi^2}{6\alpha'^2} R(\kappa, \tau), \quad \tilde{\mathcal{H}}_{\text{BY}}(\tilde{k}, \tilde{\eta}) = \frac{\pi^2}{3\alpha'^2} H(\kappa, \tau), \\ \xi_{\text{R,L,0}}(\tilde{\eta}) &= \frac{\pi \tilde{k}_{\text{max}}}{\alpha'} M_{\text{R,L,0}}(\tau), \quad \tau = \frac{2\tilde{k}_{\text{max}}^2}{\sigma_c} \tilde{\eta}, \quad \tilde{k} = \tilde{k}_{\text{max}} \kappa, \end{aligned} \quad (\text{B.1})$$

where $0 < \kappa < 1$ and $\tau \geq 0$ is the new dimensionless time. Using Eq. (B.1), we rewrite Eq. (2.1) in the form,^{22,23}

$$\begin{aligned} \frac{\partial R}{\partial \tau} &= -\kappa^2 (1 + \lambda_t I_{\text{R}}) R + \kappa^2 \left(M_{\text{R}} - \frac{M_{\text{L}}}{2} + \lambda_t I_{\text{H}} \right) H, \\ \frac{\partial H}{\partial \tau} &= -\kappa^2 (1 + \lambda_t I_{\text{R}}) H + \left(M_{\text{R}} - \frac{M_{\text{L}}}{2} + \lambda_t I_{\text{H}} \right) R, \\ \frac{dM_{\text{R}}}{d\tau} &= I_{\text{H}} - \left(M_{\text{R}} - \frac{M_{\text{L}}}{2} \right) I_{\text{R}} - \Gamma'(M_{\text{R}} - M_{\text{L}} + M_0), \\ \frac{dM_{\text{L}}}{d\tau} &= -\frac{1}{4} I_{\text{H}} + \frac{1}{4} \left(M_{\text{R}} - \frac{M_{\text{L}}}{2} \right) I_{\text{R}} - \Gamma'(M_{\text{L}} - M_{\text{R}} - M_0)/2 - \frac{\Gamma'_s}{2} M_{\text{L}}, \end{aligned}$$

$$\frac{dM_0}{d\tau} = -\Gamma'(M_R + M_0 - M_L)/2, \quad (\text{B.2})$$

where

$$I_R(\tau) = \int_0^1 d\kappa R(\kappa, \tau), \quad I_H(\tau) = \int_0^1 d\kappa \kappa^2 H(\kappa, \tau), \quad \lambda_t = \frac{2\sigma_c \tilde{k}_{\text{max}}^2 \pi^2}{9\alpha'^4(\tilde{p} + \tilde{\rho})},$$

$$\Gamma'(\tau) = \frac{121\sigma_c}{\tilde{\eta}_{\text{EW}} \tilde{k}_{\text{max}}^2} \left[1 - \frac{T_{\text{EW}}^2}{T_{\text{RL}}^2} \left(1 + \frac{T_{\text{RL}}}{M_0} \frac{\sigma_c}{2\tilde{k}_{\text{max}}^2} \tau \right)^2 \right], \quad (\text{B.3})$$

and $\Gamma'_s = \sigma_c \Gamma_{\text{sph}} / 2\tilde{k}_{\text{max}}^2$.

Appendix C. Energy spectrum of a stochastic GW background

It is convenient to characterize the spectrum of isotropic stochastic GWs by the following dimensionless function of the frequency f measured in Hz:⁴³

$$\Omega(f) = \frac{1}{\rho_{\text{crit}}} \frac{d\rho_{\text{GW}}}{d \ln f}, \quad (\text{C.1})$$

where $d\rho_{\text{GW}}$ is the energy density of GWs contained within the frequency interval $(f, f + df)$ and ρ_{crit} is the critical density of the universe defined in Sec. 3.1. Using the definition of the total conformal energy density of GWs in Eq. (3.2), we get that

$$\rho_{\text{GW}}^{(c)}(\eta) = \int_0^\infty \rho_{\text{GW}}^{(c)}(f, \eta) df = \int_0^\infty \frac{d\rho_{\text{GW}}}{df} df. \quad (\text{C.2})$$

On the basis of Eq. (C.2), one obtains that $\frac{d\rho_{\text{GW}}}{df} = \rho_{\text{GW}}^{(c)}(f, \eta)$.

Taking into account that $k = 2\pi f$ for massless gravitons, we get that $\rho_{\text{GW}}^{(c)}(f, \eta) = 2\pi \rho_{\text{GW}}^{(c)}(k, \eta)$, where $\rho_{\text{GW}}^{(c)}(k, \eta)$ is given in Eq. (3.1). Eventually, we arrive to Eq. (3.4) with $\rho_{\text{GW}}(f) \equiv \rho_{\text{GW}}^{(c)}(f, \eta)$. Since the frequency f is related to the conformal momentum k , we call it the conformal frequency.

Appendix D. Derivation of the density matrix equation for neutrino oscillations

In this appendix, we clarify some of the issues in the derivation of the equation for the density matrix of flavor neutrinos interacting with stochastic GWs. The treatment of these issues in Ref. 17 was insufficiently strict.

The evolution of the wavefunction of flavor neutrinos $\nu^T = (\nu_e, \nu_\mu, \nu_\tau)$ under the influence of stochastic GWs obeys the effective Schrödinger equation, $i\dot{\nu} = (H_f^{(0)} + H_f^{(1)})\nu$, where $H_f^{(0,1)}$ are the effective Hamiltonians for neutrino oscillations in vacuum and the contribution of stochastic GWs. The explicit form of $H_f^{(0,1)}$ is given in Refs. 15, 16, 17. We can also consider neutrino mass eigenstates ψ_a , $a = 1, 2, 3$, having the masses m_a , by making the matrix transformation, $\nu = U\psi$, where U is the 3×3 unitary matrix. The effective Hamiltonians in the mass basis are $H_m^{(0,1)} = U^\dagger H_f^{(0,1)} U$. It turns out that $H_m^{(0,1)}$ are diagonal, $(H_m^{(1,2)})_{ab} \propto \delta_{ab}$.

We can also consider the wavefunction in the interaction picture ψ' , $\psi = \exp(-iH_m^{(0)}t)\psi'$. It obeys the Schrödinger equation, $i\dot{\psi}' = H_{\text{int}}\psi'$, where $H_{\text{int}} = \exp(iH_m^{(0)}t)H_m^{(1)}\exp(-iH_m^{(0)}t) = H_m^{(1)}$ is the Hamiltonian in the interaction picture. One can prove that $H_{\text{int}} = H_m^{(1)}$ (see, e.g., Ref. 17) since both $H_m^{(0)}$ and $H_m^{(1)}$ are diagonal. If we consider stochastic external fields, instead of ψ' , it is convenient to deal with the density matrix ρ' which satisfies the equation,

$$i\dot{\rho}' = [H_m^{(1)}, \rho']. \quad (\text{D.1})$$

The initial condition for Eq. (D.1) is $\rho'(0) = U^\dagger \rho_f^{(0)} U$, where $\rho_f^{(0)}$ is the initial density matrix for flavor neutrinos. We suppose that $(\rho_f^{(0)})_{\lambda\lambda'} \propto \delta_{\lambda\lambda'} (F_\lambda)_S$, where $(F_\lambda)_S$ are the fluxes of flavor neutrinos at a source.

The formal solution of Eq. (D.1) is

$$\rho'(t) = \rho'(0) - i \int_0^t [H_m^{(1)}(t_1), \rho'(0)] dt_1 - \int_0^t \int_0^{t_1} [H_m^{(1)}(t_1), [H_m^{(1)}(t_2), \rho'(0)]] dt_1 dt_2 + \dots, \quad (\text{D.2})$$

where $H_m^{(1)} = H_m^{(1)}(t)$ is supposed to be the random function of time since we consider stochastic GWs which have randomly distributed amplitudes and cross the neutrino trajectory at random angles. GW can have two independent polarizations: ‘plus’ and ‘times’. Thus, we separate the effective Hamiltonian into two parts, $H_m^{(1)} = H_{m,+}^{(1)} + H_{m,\times}^{(1)}$, which are uncorrelated. After averaging Eq. (D.2), one gets

$$\begin{aligned} \langle \rho' \rangle(t) = & \rho'(0) - \int_0^t \int_0^{t_1} \left[\langle H_{m,+}^{(1)}(t_1), [H_{m,+}^{(1)}(t_2), \rho'(0)] \rangle \right] dt_1 dt_2 \\ & - \int_0^t \int_0^{t_1} \left[\langle H_{m,\times}^{(1)}(t_1), [H_{m,\times}^{(1)}(t_2), \rho'(0)] \rangle \right] dt_1 dt_2 + \dots \end{aligned} \quad (\text{D.3})$$

Let us consider, e.g., the term containing the ‘plus’ correlator in Eq. (D.3). Using the results of Ref. 17, we have

$$\left(H_{m,+}^{(1)} \right)_{ab} = -\frac{p^2}{2E_a} \delta_{ab} h_+ \sin^2 \vartheta \cos 2\varphi \cos \phi_a, \quad (\text{D.4})$$

where $\phi_a = \omega t(1 - v_a \cos \vartheta)$ is the phase of GW accounting for the intersection of the direction of the GW propagation and the neutrino trajectory, $v_a = p/E_a$ is the velocity of the neutrino mass eigenstate, $E_a = \sqrt{m_a^2 + p^2}$ is the energy of the neutrino mass eigenstate, p is the momentum of neutrinos, ϑ and φ are the angles fixing the neutrino momentum with respect to the wave vector of GW, which is supposed to propagate along the z -axis.

In the averaging procedure in Eq. (D.3), one has to deal with the binary combination of the components of $H_{m,+}^{(1)}$. Thus, accounting for Eq. (D.4), we should consider the mean value

$$\begin{aligned} & \frac{p^4}{4E_a E_b} \langle h'_+ h''_+ \sin^2 \vartheta' \sin^2 \vartheta'' \cos 2\varphi' \cos 2\varphi'' \cos \phi'_a \cos \phi''_b \rangle \\ & = \frac{p^4}{4E_a E_b} \langle h'_+ h''_+ \rangle \langle \sin^2 \vartheta' \sin^2 \vartheta'' \cos 2\varphi' \cos 2\varphi'' \cos \phi'_a \cos \phi''_b \rangle, \end{aligned} \quad (\text{D.5})$$

where prime and double prime correspond to different moments of time t' and t'' . Also, we separated the mean values of the amplitudes and the angular factors. The correlator of the amplitudes $\langle h'_+ h''_+ \rangle = f_+(t' - t'')$ is the arbitrary function depending on the source of GWs. In Sec. 4, we relate it to the spectral density of GW; cf. Eq. (4.3).

We assume that random angles ϑ and φ are δ -function correlated. It is a reasonable assumption since sources of GWs are distributed randomly. Thus, in Eq. (D.5), we obtain that

$$\begin{aligned} & \langle \sin^2 \vartheta' \sin^2 \vartheta'' \cos 2\varphi' \cos 2\varphi'' \cos \phi'_a \cos \phi''_b \rangle \rightarrow \langle \sin^4 \vartheta \cos^2 2\varphi \cos \phi_a \cos \phi_b \rangle \\ & = \int_0^{2\pi} \frac{d\varphi}{2\pi} \cos^2 2\varphi \int_0^\pi \frac{d\vartheta}{\pi} \sin^4 \vartheta \cos[\omega t(1 - v_a \cos \vartheta)] \cos[\omega t(1 - v_a \cos \vartheta)]. \end{aligned} \quad (\text{D.6})$$

The integral over ϑ in Eq. (D.7) reads

$$\begin{aligned} I_{ab} &= \frac{1}{2} \int_0^\pi \frac{d\vartheta}{\pi} \sin^4 \vartheta [\cos(\delta_{ab} \cos \vartheta) + \cos(2\omega t) \cos(\sigma_{ab} \cos \vartheta) + \sin(2\omega t) \sin(\sigma_{ab} \cos \vartheta)] \\ &= \frac{3}{16} [I_c(\delta_{ab}) + \cos(2\omega t) I_c(\sigma_{ab}) + \sin(2\omega t) I_s(\sigma_{ab})], \end{aligned} \quad (\text{D.7})$$

where $\delta_{ab} = (v_a - v_b)\omega t$ and $\sigma_{ab} = (v_a + v_b)\omega t$. The integrals in Eq. (D.7) are¹⁵

$$\begin{aligned} I_c(\lambda) &= \frac{8}{3\pi} \int_0^\pi d\vartheta \sin^4 \vartheta \cos(\lambda \cos \vartheta) = \frac{8}{\lambda^3} [2J_1(\lambda) - \lambda J_0(\lambda)], \\ I_s(\lambda) &= \frac{8}{3\pi} \int_0^\pi d\vartheta \sin^4 \vartheta \sin(\lambda \cos \vartheta) = 0, \end{aligned} \quad (\text{D.8})$$

where $J_{0,1}(\lambda)$ are the Bessel functions.

In Sec. 3.1, we find that the spectral function Ω for relic GWs produced by random HMFs reaches its maximal values in a plateau with the the frequencies range from \sim Hz to \sim kHz (see, e.g., Table 1). Thus, if study the interaction of SN neutrinos with such stochastic GWs, we get that the quantities in Eq. D.7 are

$$\begin{aligned} \min(\sigma_{ab}) &= 2\omega_{\min} L = 1.3 \times 10^{13} \gg 1, \\ \max(\delta_{ab}) &= \omega_{\max} L \frac{\Delta m_{31}^2}{2E^2} = 8.3 \times 10^{-2} \ll 1, \end{aligned} \quad (\text{D.9})$$

where $L = 10$ kpc is the neutrino propagation distance comparable with the galaxy size (see Ref. 17 and Sec. 4) and $E = 10$ MeV is the typical SN neutrino energy. We take $\Delta m_{31}^2 = m_3^2 - m_1^2 = 2.55 \times 10^{-3} \text{ eV}^{244}$ in Eq. (D.9) since it is the maximal mass squared difference.

Using the estimates in Eq. (D.9), one gets that $I_c(\lambda) \rightarrow 1$ if $\lambda \ll 1$ and $I_c(\lambda) \rightarrow 0$ if $\lambda \gg 1$. Thus, $I_{ab} \rightarrow \frac{3}{16}$ in Eq. (D.7). It is important that the leading order in I_{ab} is independent of the indexes a and b , as well as of time. It means that, effectively, we can set $v_a \rightarrow 1$ in ϕ_a . The same result is obtained while averaging $\langle H_{m,\times}^{(1)}(t_1) H_{m,\times}^{(1)}(t_2) \rangle$. The present averaging over the angles ϑ and φ is careful, whereas the analysis in Ref. 17 was insufficiently strict.

Finally, Eq. (D.3) is rewritten in the form,

$$\begin{aligned} \langle \rho' \rangle (t) = & \rho'(0) - \frac{3}{128} [H_m^{(0)}, [H_m^{(0)}, \rho'(0)]] \\ & \times \int_0^t \int_0^{t_1} (\langle h_+(t_1) h_+(t_2) \rangle + \langle h_\times(t_1) h_\times(t_2) \rangle) dt_1 dt_2 + \dots, \end{aligned} \quad (\text{D.10})$$

where $H_m^{(0)} = \frac{1}{2E} \text{diag}(0, \Delta m_{21}^2, \Delta m_{31}^2)$ is the effective Hamiltonian for vacuum oscillations. This series in Eq. (D.10) is a formal solution of the following differential equation:

$$\begin{aligned} \frac{d}{dt} \langle \rho' \rangle (t) = & -g[H_m^{(0)}, [H_m^{(0)}, \langle \rho' \rangle (t)]], \\ g(t) = & \frac{3}{128} \int_0^t (\langle h_+(t) h_+(t_1) \rangle + \langle h_\times(t) h_\times(t_1) \rangle) dt_1. \end{aligned} \quad (\text{D.11})$$

Applying the formalism developed in Ref. 17 to Eq. (D.11), we obtain the probabilities in Eq. (4.1).

References

1. A. Neronov and I. Vovk, *Science* **328** (2010) 73, arXiv:1006.3504.
2. R. Durrer and A. Neronov, *Astron. Astrophys. Rev.* **21** (2013) 62, arXiv:1303.7121.
3. K. Subramanian, *Rep. Prog. Phys.* **79** (2016) 076901, arXiv:1504.02311.
4. M. Joyce and M. Shaposhnikov, *Phys. Rev. Lett.* **79** (1997) 1193, astro-ph/9703005.
5. M. Dvornikov and V. B. Semikoz, *Phys. Rev. D* **87** (2013) 025023, arXiv:1212.1416.
6. K. Kamada and A. Long, *Phys. Rev. D* **94** (2016) 063501, arXiv:1606.08891.
7. K. Fukushima, D. E. Kharzeev and H. J. Warringa, *Phys. Rev. D* **78** (2008) 074033, arXiv:0808.3382.
8. A. Boyarsky, J. Fröhlich and O. Ruchayskiy, *Phys. Rev. Lett.* **108** (2012) 031301 arXiv:1109.3350.
9. A. Boyarsky, V. Cheianov, O. Ruchayskiy and O. Sobol, *Phys. Rev. D* **103** (2021) 013003, arXiv:2008.00360.
10. A. Kosowsky, A. Mack and T. Kahniashvili, *Phys. Rev. D* **66** (2002) 024030, astro-ph/0111483.
11. A. Brandenburg, Y. He, T. Kahniashvili, M. Rheinhardt and J. Schober, *Astrophys. J.* **911** (2021) 110, arXiv:2101.08178.
12. C. Caprini and D. G. Figueroa, *Class. Quantum Grav.* **35** (2018) 163001, arXiv:1801.04268.
13. LIGO Scientific Collab. and Virgo Collab. (B. P. Abbott *et al.*), *Phys. Rev. Lett.* **116** (2016) 061102, arXiv:1602.03837.
14. NANOGrav Collab. (Z. Arzoumanian *et al.*), *Astrophys. J. Lett.* **905** (2020) L34, arXiv:2009.04496.
15. M. Dvornikov, *Phys. Rev. D* **100** (2019) 096014, arXiv:1906.06167.
16. M. Dvornikov, *J. Cosmol. Astropart. Phys.* **12** (2020) 022 arXiv:2009.02195.
17. M. Dvornikov, *Phys. Rev. D* **104** (2021) 043018, arXiv:2103.15464.
18. G. Koutsoumbas and D. Metaxas, *Gen. Rel. Grav.* **52** (2020) 102, arXiv:1909.02735.
19. ANTARES, IceCube, LIGO, Virgo Collabs. (A. Albert *et al.*), *Astrophys. J.* **870** (2019) 134, arXiv:1810.10693.
20. IceCube Collab. (M. G. Aartsen *et al.*), *Astrophys. J. Lett.* **898** (2020) L10, arXiv:2004.02910.

21. E. Vitagliano, I. Tamborra and G. Raffelt, *Rev. Mod. Phys.* **92** (2020) 045006, arXiv:1910.11878.
22. M. Dvornikov and V. B. Semikoz, *Eur. Phys. J. C* **81** (2021) 1001, arXiv:2110.01071.
23. M. Dvornikov, *J. Cosmol. Astropart. Phys.* **01** (2022) 021, arXiv:2110.04214.
24. M. Giovannini and M. E. Shaposhnikov, *Phys. Rev. D* **57** (1998) 2186, hep-ph/9710234.
25. V. B. Semikoz, A. Yu. Smirnov and D. D. Sokoloff, *Phys. Rev. D* **93** (2016) 103003, arXiv:1604.02273.
26. B. A. Campbell, S. Davidson, J. Ellis and K. A. Olive, *Phys. Lett. B* **297** (1992) 118, [hep-ph/9302221].
27. D. S. Gorbunov and V. A. Rubakov, *Introduction to the Theory of the Early Universe: Hot Big Bang Theory* (World Scientific, Singapore, 2011), p. 250.
28. L. Campanelli, *Phys. Rev. Lett.* **98** (2007) 251302, arXiv:0705.2308.
29. M. Dvornikov and V. B. Semikoz, *Phys. Rev. D* **95** (2017) 043538, arXiv:1612.05897.
30. A. Brandenburg, T. Kahniashvili, S. Mandal, A. Roper Pol, A. G. Tevzadze and T. Vachaspati, *Phys. Rev. D* **96** (2017) 123528, arXiv:1711.03804.
31. LIGO Scientific Collab., Virgo Collab., KAGRA Collab. (R. Abbott *et al.*), *Phys. Rev. D* **104** (2021) 022004, arXiv:2101.12130.
32. B. Cheng, D. N. Schramm and J. W. Truran, *Phys. Rev. D* **49** (1994) 5006, astro-ph/9308041.
33. K. Kamada, F. Uchida and J. Yokoyama, *J. Cosmol. Astropart. Phys.* **04** (2021) 034, arXiv:2012.14435.
34. M. M. Anber and E. Sabancilar, *Phys. Rev. D* **92** (2015) 101501, arXiv:1507.00744.
35. M. C. Guzzetti, N. Bartolo, M. Liguori and S. Matarrese, *Riv. Nuovo Cim.* **39** (2016) 399, arXiv:1605.01615.
36. V. K. Oikonomou, *Astropart. Phys.* **141** (2022) 102718, arXiv:2204.06304.
37. V. K. Oikonomou, *Astropart. Phys.* **144** (2023) 102777, arXiv:2209.09781.
38. V. K. Oikonomou, *Nucl. Phys. B* **984** (2022) 115985, arXiv:2210.02861.
39. S. D. Odintsov, V. K. Oikonomou and R. Myrzakulov, *Symmetry* **14** (2022) 729, arXiv:2204.00876.
40. BICEP/Keck Collab. (P. A. R. Ade *et al.*), *Phys. Rev. Lett.* **127** (2021) 151301, arXiv:2110.00483.
41. LISA Collab. (P. Auclair *et al.*), arXiv:2204.05434.
42. G. Sigl, *Phys. Rev. D* **66** (2002) 123002, astro-ph/0202424.
43. B. Allen and A. C. Ottewill, *Phys. Rev. D* **56** (1997) 545, gr-qc/9607068.
44. P. F. de Salas, D. V. Forero, S. Gariazzo, P. Martínez-Miravé, O. Mena, C. A. Ternes, M. Tórtola and J. W. F. Valle, *J. High Energy Phys.* **02** (2021) 071, arXiv:2006.11237.